



## Occurrence and orientation of anorbital ripples in near-shore sands

Irene Maier<sup>1</sup> and Alex E. Hay<sup>1</sup>

Received 28 July 2008; revised 22 July 2009; accepted 6 August 2009; published 10 December 2009.

[1] The orientation of linear transition ripples (LTRs) relative to incident wave direction is studied using rotary fan beam sonar images and wave and current data from electromagnetic flowmeters in  $\sim 3$  m water during SandyDuck97. LTR occurrence is determined objectively with an automatic recognition algorithm. LTRs occurred for RMS wave orbital velocities between 0.15 and 0.35 m s<sup>-1</sup>. The ripples were highly two dimensional, and of the anorbital type ( $\lambda_0/D_{50} = 524$  to 535,  $d_0/D_{50} = 4300$  to 25,000) with 7.6 cm mean wavelength in 150  $\mu$ m median diameter sand. The ripple crests were typically aligned perpendicular to the incident sea-and-swell direction: specifically, about 60% of the normals to the crests differ from wave direction by less than 5° and more than 90% by less than 10°. During rapid changes in wave direction, however, ripple orientation adjustment lagged the wave direction by O(1 h). Ripple reorientation occurred piecewise along the crests, with new crest segments sometimes bridging two or more old segments. The 1 h reorientation time scale is longer by several orders of magnitude than the adjustment time based on theoretical bed load transport rate and the ripple volume. As a possible explanation, we suggest that a significant fraction of the transport, more than 90%, bypasses the ripples during orientation adjustment through large angles.

**Citation:** Maier, I., and A. E. Hay (2009), Occurrence and orientation of anorbital ripples in near-shore sands, *J. Geophys. Res.*, 114, F04022, doi:10.1029/2008JF001126.

### 1. Introduction

[2] Wave-formed ripple geometry depends on grain size and the properties of the near-bottom wave motion. Clifton [1976] and Clifton and Dingler [1984] introduced a classification scheme involving three primary ripple types based on ripple wavelength,  $\lambda$ , and near-bed wave orbital excursion,  $d_0$ , each nondimensionalized by median grain size,  $D_{50}$ . Ordered by increasing wave orbital excursion, the three types were designated as orbital, suborbital, and anorbital ripples. Only the latter type is considered here. Wiberg and Harris [1994] have revisited this classification scheme, obtaining revised estimates of the parameter ranges for the different categories. Anorbital ripples occur for values of  $d_0/D_{50}$  between 3000 and 20,000. Ripple wavelength is independent of the orbital excursion, and  $\lambda/D_{50} \sim 535$  on average. Thus, anorbital ripple wavelengths are much shorter than the near-bed wave orbital excursions.

[3] Linear transition ripples (LTRs) are two-dimensional, long-crested, low-relief ripples of the anorbital type [Conley and Inman, 1992]. (A more specific definition is given in section 3.2.) The first field observations of LTRs were the “ephemeral” ripples reported by Inman [1957]. Subsequently, LTRs have been reported in field observations by

Dingler and Inman [1977], Conley and Inman [1992], Hay and Wilson [1994], Crawford and Hay [2001], Smyth et al. [2002], and Hay and Mudge [2005]. LTRs occur at moderate to high wave energies, just below the transition to and from flat bed [Conley and Inman, 1992; Crawford and Hay, 2001; Hay and Mudge, 2005]. Typical LTR heights are a few mm [Dingler and Inman, 1977; Crawford and Hay, 2001], and since wavelengths are 10 cm or less, typical steepnesses are 0.05 or less. Of the five principal bed states during SandyDuck97 reported by Hay and Mudge [2005], LTRs were the most frequent.

[4] The primary purpose of this paper is to investigate LTR orientation as a function of incident wave direction. Motivation for studying ripple orientation stems from the fact that the time dependence of orientation adjustment has received very little attention. This lack of data on ripple orientation adjustment led Soulsby and Whitehead [2005] to assume that the characteristic response times for ripple height and wavelength could be applied to orientation. This assumption needs to be tested. Laboratory experiments on wave-generated ripple orientation are difficult to carry out because of scale constraints, particularly in the anorbital range. We have chosen to focus on LTR orientation for several reasons: (1) their long crestedness allows for relatively precise orientation estimates; (2) their frequent occurrence in the SandyDuck97 data set provides multiple realizations; (3) their low amplitude and steepness suggest a relatively fast response. With regard to the last point, according to the observations of Dingler and Inman

<sup>1</sup>Department of Oceanography, Dalhousie University, Halifax, Nova Scotia, Canada.

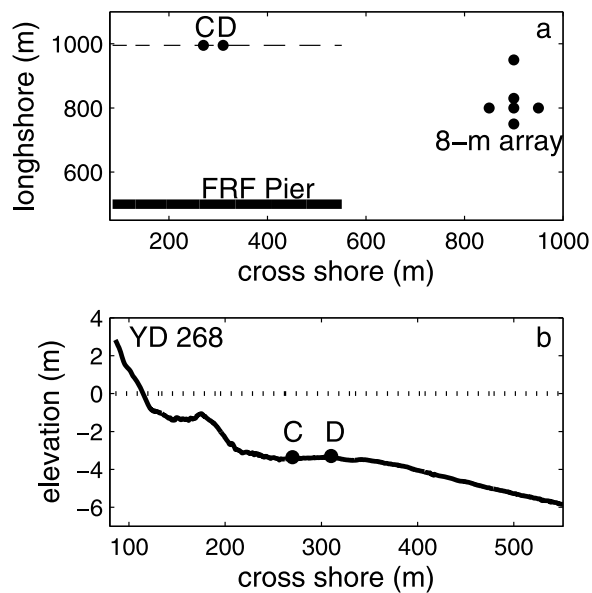


**Figure 1.** (a) Plan view of the FRF field site showing the locations of the instrument frames C and D as well as the 8 m offshore array. (b) Bathymetric profile on yearday 268. The dashed line in Figure 1a indicates the location of the bathymetric profile in Figure 1b. Distances are in the FRF coordinate system.

[1977] and Conley and Inman [1992], LTRs can be eroded and reformed within a wave cycle. Based on this result, one might expect that only a few wave cycles would be required for these ripples to become aligned with the waves forming them, leading to the hypothesis that LTR orientation should closely follow the wave direction. Our principal goal is to test this hypothesis.

[5] The paper is organized as follows. A description of the data set and an outline of the data analysis methods are presented in section 2, including the automatic recognition algorithm for identifying LTRs in rotary sonar images, and the techniques used to determine ripple orientation, ripple wavelength, and wave direction. The results are presented in section 3, beginning with LTR occurrence relative to the forcing conditions in section 3.1. The observed ripple wavelengths are discussed relative to wave orbital diameter in section 3.2, highlighting an outstanding discrepancy between field and large-scale laboratory results in the anorbital ripple range. Ripple crest orientations and wave directions are compared in section 3.3. Section 4 is a discussion of ripple adjustment time scales, including results from laboratory experiments, in which a discrepancy of several orders of magnitude between the observed and predicted time scale is identified, and a possible rationale for the discrepancy suggested. The conclusions of this study are summarized in section 5.

## 2. Data and Methods

### 2.1. Field Site and Data

[6] SandyDuck97 took place at the U.S. Army Corps of Engineers Field Research Facility (FRF) near Duck, North Carolina from August to November 1997. Figure 1 shows the instrument locations of interest here, frames C and D

and the FRF 8m array, relative to the FRF pier and a representative cross-shore bathymetric profile. The median grain size was  $145 \mu\text{m}$  and  $148 \mu\text{m}$  at frame C and D, respectively [Hay and Mudge, 2005]. Water velocity was measured at each frame with Marsh-McBirney electromagnetic (EM) flowmeters mounted at a nominal height of 0.5 m above the bed. The flowmeters were sampled continuously at 2 Hz, and records were stored at half hour intervals [Henderson and Bowen, 2002]. Bed state was monitored using 2.25 MHz Kongsberg Mesotech Model 971 rotary fan beam sonars mounted at a nominal height of 0.75 m above bottom. The sonar images were acquired at 10 min intervals during storm events and at 30 min intervals during the less active transport conditions between storms.

[7] The coordinate system used here is sketched in Figure 2. The  $x$  direction and the  $u$  component of the velocity are positive shoreward, the  $y$  direction and  $v$  are alongshore and positive southward. The wave incidence angle,  $\alpha$ , is defined such that positive angles of incidence indicate wave directions from the northeast quadrant, negative angles from the southeast. Shore normal incidence corresponds to  $\alpha = 0^\circ$ .

[8] The rotary sonars were mounted on a cantilevered mast extending horizontally eastward and northward at a nominal angle of  $60^\circ$  from shore normal, in order to place the sensors away from the influence of the frame, which was in turn attached to 4 vertical steel pipes jettied deeply into the sand [Hay and Mudge, 2005]. The acoustic images were locked to the frame leg positions with an accuracy of  $\pm 1^\circ$  by cross correlating the range azimuth images to a template of the frame elements with the well-defined echoes from the frame legs. Frame orientation with respect to the shore normal was determined by least squares fitting the surveyed  $xy$  positions of the tops of the pipes to the known frame geometry. The resulting RMS orientation error is  $\pm 4^\circ$ . The resulting frame orientation angles were used to register the sonar images and flowmeter measurements relative to shore normal. For detailed information on the sonar image processing, the reader is referred to Hay and Mudge [2005].

### 2.2. Automatic Recognition of Linear Transition Ripples

[9] A typical sonar image showing LTRs is presented in Figure 3. LTRs are evident as the  $O(10 \text{ cm})$  wavelength, shore-parallel features within approximately  $\pm 30^\circ$  of shore

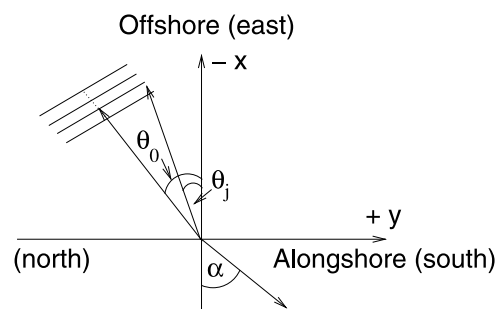


**Figure 2.** Coordinate system. Here  $\theta_0$  is the ripple crest orientation (normal to the ripple crests, the parallel lines),  $\theta_j$  is the azimuth angle of the sonar beam, and  $\alpha$  is the incident wave direction. Angles are positive counterclockwise relative to the  $x$  axis.

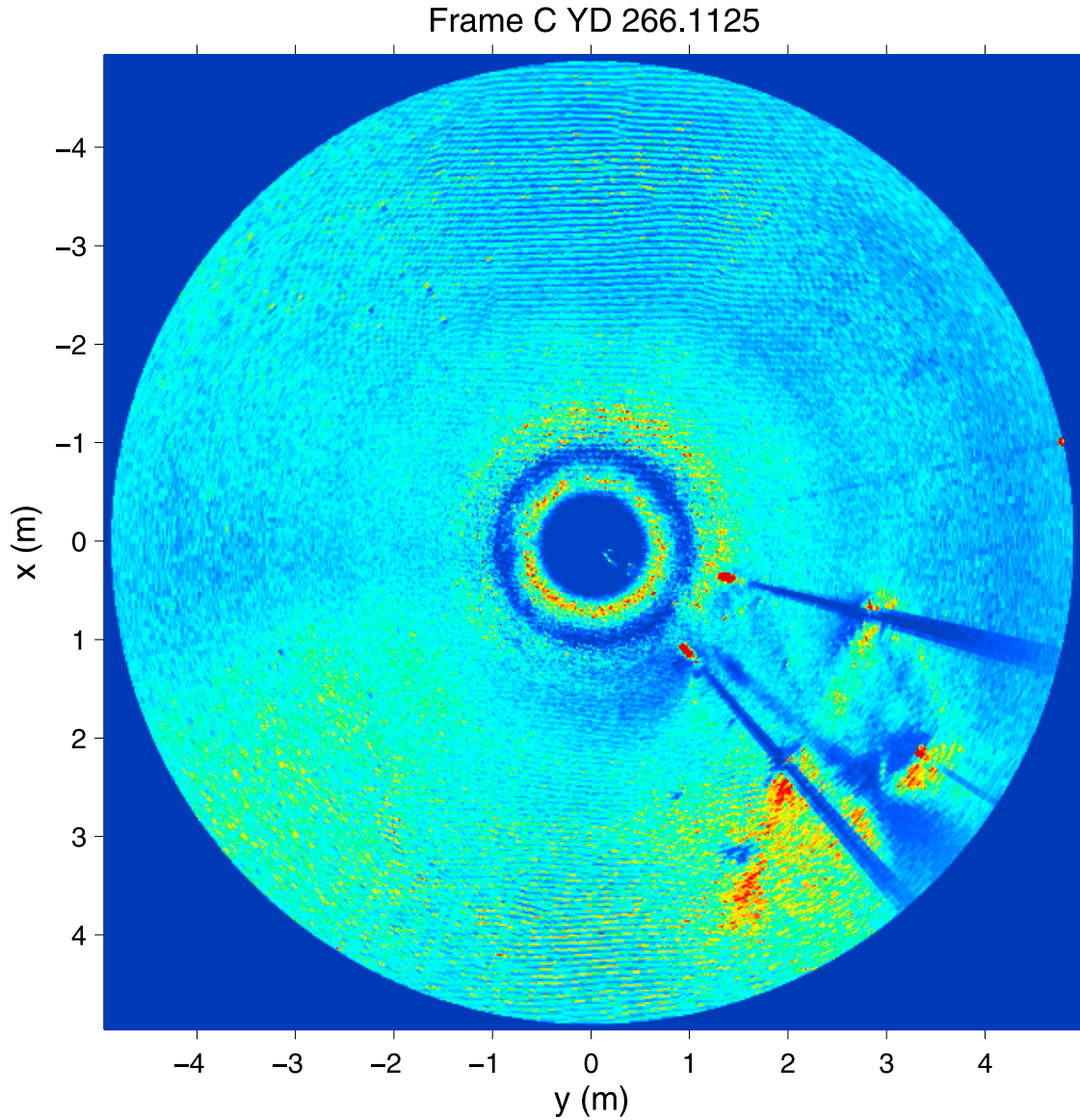


**Figure 3.** Rotary fan beam image from frame C on yearday 266.1125. Positive  $x$  is in the onshore (westward) direction, positive  $y$  is in the alongshore (southward) direction. Red denotes high backscatter; blue denotes low backscatter. Note the shadows cast by the instrument frame in the lower right quadrant. Linear transition ripples are visible on the offshore and onshore sides between  $x = -2$  and  $-5$  m, and  $x = 2$  and  $5$  m, respectively.

normal on the offshore and onshore sides of the image. In the alongshore direction, the ripples are not imaged because the acoustic beam intersects the ripple profile parallel to the crestlines, and there is no crest-to-trough contrast in backscatter amplitude. In the intermediate regions (i.e., just beyond  $\pm 30^\circ$ ), a Moiré-type pattern can be seen, consisting of arcs cutting across the ripple pattern. These arcs are an artifact of the range azimuth data to Cartesian coordinates. In the regions where they are imaged clearly, and through the Moiré affected areas (as best seen by viewing the image from the side), the ripples are highly two dimensional.

[10] In their analysis of the bed states during Sandy-Duck97, Hay and Mudge [2005] identified a distinctive feature of linear transition ripples: their highly anisotropic

radial seabed backscatter spectra, which is a direct consequence of the two dimensionality of the ripple pattern. Figure 4 presents a typical LTR radial backscatter spectrum, designated by  $S_{bb}(f, \theta)$ ,  $f$  being the spatial frequency and  $\theta$  the azimuthal angle. High spectral density lobes in the 10 to 20 cpm (cycles per meter) spatial frequency band are present on the offshore and onshore sides of the frame. Using this particular property, an algorithm was devised to assign LTR occurrences automatically while excluding other bed states.  $S_{bb}$  was averaged over a  $\pm 30^\circ$  range of angles ( $\Delta\theta$ ) and the 10–20 cpm frequency range ( $\Delta f$ ) to obtain

$$\sigma_A(\Delta f, \Delta\theta) = \frac{1}{N} \sum_{ij} S_{bb}(f_i, \theta_j) \quad (1)$$

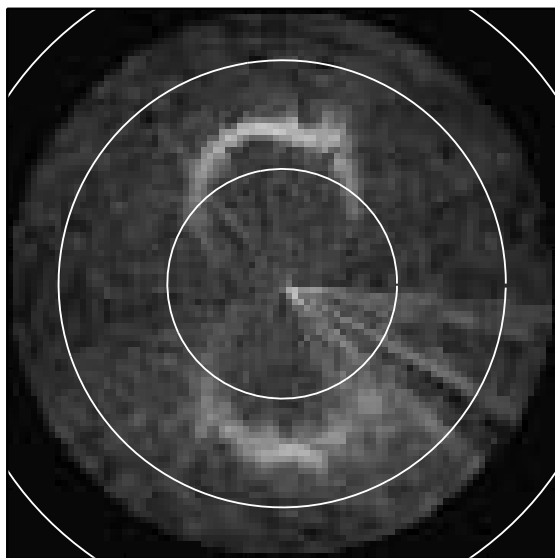


**Figure 4.** Radial backscatter spectrum versus azimuth for the sonar image in Figure 3. Note the high spectral density lobes on the seaward (top) and shoreward (bottom) sides and the low backscatter levels in the alongshore direction (left, away from the frame). White circles indicate spatial frequency at 10 cpm intervals.

where  $N$  is the number of points in the area spanned by  $\Delta\theta$  and  $\Delta f$ , and thus  $\sigma_A$  is proportional to the variance. Similarly  $\sigma_B$  was calculated in the northward (alongshore) direction between  $-60^\circ$  and  $-120^\circ$ , but in the 3–10 cpm frequency band. LTRs were determined to be present if  $\sigma_A$  was larger than a specified threshold, and  $\sigma_B$  smaller than a second threshold value. Different thresholds were used for the two frames, because the sensitivities and noise levels for the two sonars were different. The thresholds were also adjusted with time to account for gradual deterioration in sensitivity over the course of the experiment, which occurred for the frame D sonar especially.

[11] Table 1 summarizes the number of LTR occurrences detected by the automatic and visual methods. The automatic method detected 1300 and 708 occurrences at frames C and D, respectively, compared to 2964 and 3024 occurrences by the visual method. The algorithm finds fewer occurrences, because the visual record includes co-occurrences with other ripple types. In addition, there were images with very low backscatter in which LTRs can be seen by eye, but the peak intensities were too low to meet the automatic selection criteria. Furthermore, the automatic method uses only the offshore half of the image, and neglects any images for which LTRs were present only on the onshore side. The automatic method did detect LTRs in some instances when the visual method did not. Visual reexamination of the sonar images for these time periods confirmed that LTRs were indeed present. These instances were added to the LTR data set analyzed here, which includes only the automatic detections.

### 2.3. Ripple Orientation and Wavelength

[12] The range azimuth backscatter data produced by the sonars were converted to Cartesian coordinates at  $0.9 \times 0.9$  cm resolution, determined by the resolution in range (0.7 cm for the 10  $\mu$ s pulse length). The fixed resolution in

azimuth ( $0.8^\circ$ ) causes the cross-beam resolution to vary with range, from 1.4 cm at 1 m to 7 cm at 5 m).

[13] LTR orientations were determined by applying the Radon transform to a  $1.9 \times 3.6$  m rectangular subimage from the offshore half of each image in which LTRs were present (Figures 5a and 5c). Only the offshore part of each image was used because it is less affected by the presence of the frame. The resulting matrix of intensity values was high-pass filtered (third-order Butterworth, 5 cpm cutoff frequency) in the  $x$  direction. The Radon transform [Gindikin, 1992; Park et al., 2004] was then applied to this filtered matrix. From the variance of the Radon transform, the ripple orientation angle,  $\theta_0$ , was defined as the intensity weighted mean between the half power points on either side of the maximum variance, as illustrated for two cases in Figure 5. The corresponding ripple orientations are indicated. The full width at half maximum,  $FWHM_{\theta}$ , defined as the width of the peak at the half power points of the variance spectrum of the Radon transform, provides a measure of the uncertainty in  $\theta_0$ .

[14] Comparisons between ripple orientation and wave direction indicated a systematic difference of  $\sim 5^\circ$  [Maier, 2008]. Cheel and Hay [2008] found a similar bias between wave direction and the cross ripple bisector. This  $5^\circ$  bias has been removed from the ripple orientations presented here.

[15] Ripple wavelengths were determined from the lagged autocorrelation function ( $R_{rr}$ ) of the backscatter intensity as a function of radial distance in the  $\theta_0$  direction. The intensity data were first high-pass filtered with a fifth-order Butterworth filter with an 8 cpm cutoff frequency. The filtered intensities were averaged over a  $\pm 1^\circ$  azimuth interval, normalized by the standard deviation, then slant range corrected and linearly interpolated to an equal spacing of 0.2 cm. The separation between adjacent peaks in the autocorrelation function was defined to be the ripple wavelength,  $\lambda_0$ .

### 2.4. Incident Wave Direction

[16] The dominant wave direction,  $\alpha$ , was determined from the EM flowmeter data following Fofonoff [1969] (see also Herbers et al. [1999])

$$\tan 2\alpha = \frac{2\langle u_w v_w \rangle}{\langle u_w^2 \rangle - \langle v_w^2 \rangle} \quad (2)$$

where  $u_w$  and  $v_w$  are the horizontal ( $x$  and  $y$ , respectively) velocity components in the sea-and-swell band (0.05–0.3 Hz), and the brackets denote time averages over the 1/2 h flowmeter runs. (Note that throughout this paper, the properties of the incident surface gravity waves, such as

**Table 1.** Comparison of Linear Transition Ripple Occurrences as Detected by the Visual and Automatic Methods for Both Instrument Frames

	Frame C	Frame D
Visual		
LTR occurrences	2964	3024
LTR cross ripple co-occurrences	551	718
LTR megaripple co-occurrences	519	334
Automatic		
LTR occurrences	1300	708
LTR cross ripple co-occurrences	84	47
LTR megaripple co-occurrences	189	34

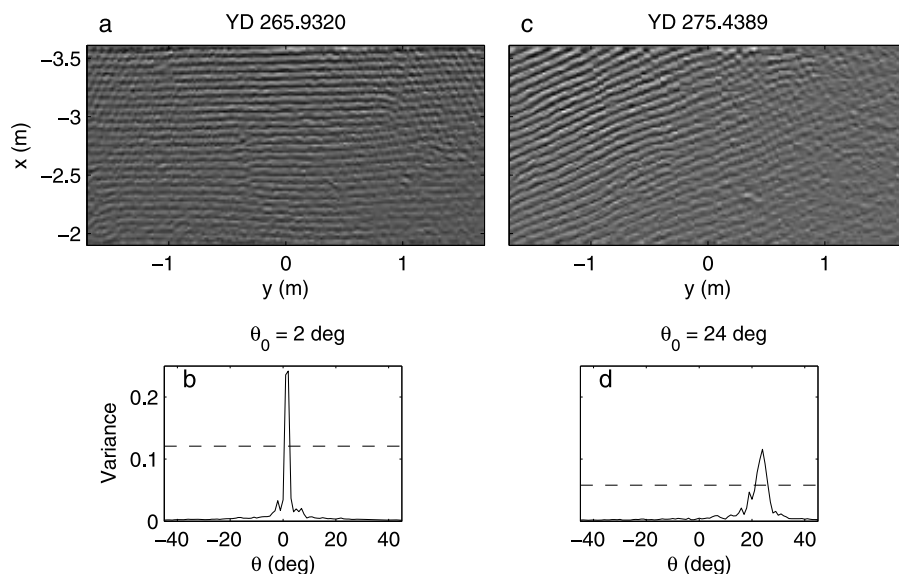


**Figure 5.** Examples of the Radon transform procedure for determining ripple orientation. (a and c) Rectangular subimages. (b and d) Variance of the Radon transform versus angle, the calculated ripple direction  $\theta_0$  corresponding to maximum variance, and the half power points (used in the uncertainty estimates).

energy and direction, are defined to be those of the sea-and-swell band at the location of the instrument frame.) As a check, incident wave directions were also determined from the wave directional spectra registered by the FRF's pressure sensor array located in 8 m water depth (Figure 1). These spectra were corrected for refraction using Snell's law, and shoaled to the frame locations assuming linear wave theory and constant cross-shore energy flux. The wave height spectrum was then transformed to near-bottom velocities using linear wave theory as described by *Cheel and Hay* [2008]. The resulting wave direction,  $\alpha_p$ , corresponds to the direction of maximum energy in the shoaled and transformed directional spectrum. The FRF runs were  $\sim 2.3$  h long and were collected every 3 h. The shoaled 8 m array wave directions are compared to directions from the EM flowmeters in Figure 6. While the  $\alpha_p$  values are somewhat more scattered, and exhibit a larger range than the values of  $\alpha$ , the two different wave direction estimates are

well correlated and in good agreement on average, especially at frame C.

### 3. Results

#### 3.1. Hydrodynamic Forcing Conditions and LTR Occurrence

[17] Time series of root-mean-square wave orbital velocity,  $u_{rms}$ , and longshore and cross-shore currents ( $v_c$ ,  $u_c$ ) at frame C are shown in Figure 7. The RMS wave orbital velocity is defined as  $u_{rms} = \sqrt{\langle u_w^2 \rangle + \langle v_w^2 \rangle}$ , and the significant wave orbital velocity as  $u_{1/3} = 2u_{rms}$  following *Thornton and Guza* [1983]. The mean currents are represented by  $u_c$  and  $v_c$ . Values for these quantities were computed from each half hour flowmeter run.

[18] The data record in Figure 7 encompasses 12 distinct major wave forcing events during which  $2u_{rms}$  exceeded  $0.5 \text{ m s}^{-1}$ . As indicated in Figure 7, LTRs occurred

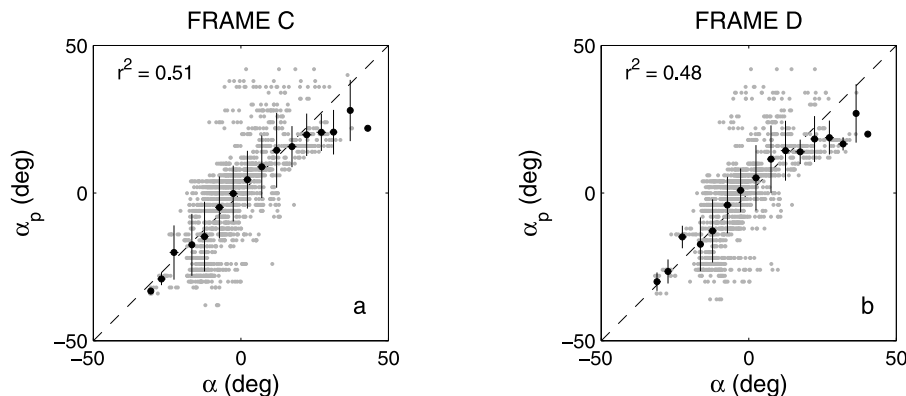


**Figure 6.** Scatterplots of shoaled FRF wave directions and EM flowmeter wave directions during SandyDuck 97 for (a) frame C and (b) frame D. The  $r^2$  values are based on the individual data points (grey); the error bars represent  $\pm 1$  standard deviation from the averages (solid black circles) over  $5^\circ$ -wide intervals in  $\alpha$ .

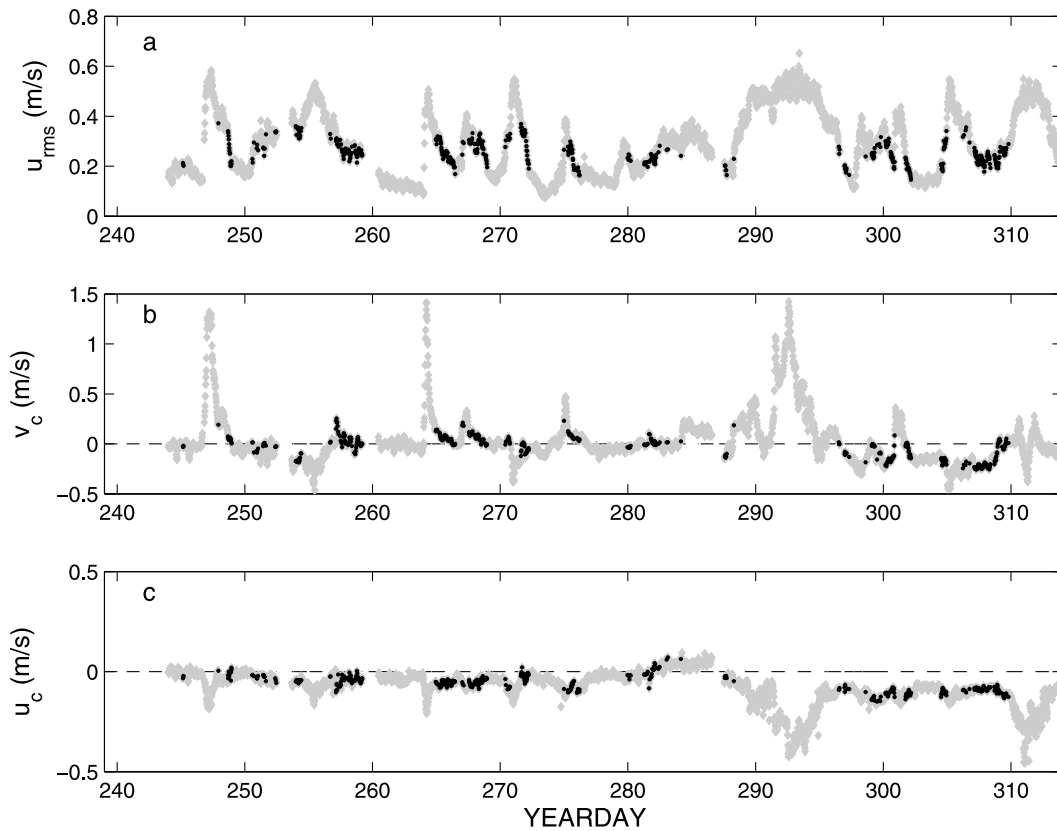


**Figure 7.** Time series of hydrodynamic forcing at frame C for the complete record showing (in grey) (a) RMS wave orbital velocity,  $u_{rms}$  (b) the longshore current,  $v_c$ , and (c) the cross-shore current,  $u_c$ . Linear transition ripple occurrences as determined by the automatic method are indicated in black.

during both the wave energy growth and decay stages for each of these events, as part of the bed state storm cycle [Hay and Mudge, 2005]. The average values of the forcing parameters during LTR occurrences are summarized in Table 2. Wave energies were moderate to high ( $2u_{rms} \sim 0.5 \text{ m s}^{-1}$ ), and longshore and cross-shore current speeds were weak. Infragravity wave velocities were also weak; that is, with the infragravity band defined as  $5 \times 10^{-4}$  to 0.05 Hz,  $u_{IG}$ , the root-mean-square infragravity wave velocity, was  $\leq 0.05 \text{ m s}^{-1}$ . These average values correspond closely to those given by Hay and Mudge [2005] for LTR occurrences based on the visual detection method.

[19] We define an LTR “occurrence” to be a single detection of LTRs by the automatic recognition algorithm. An LTR “event” is defined to be a series of occurrences during the growth or waning stages of a storm. Roughly 20 such events were observed at each frame (Figure 7). LTR “persistence” is defined to be the duration of consecutive LTR occurrences. Excluding single occurrences, the values of persistence were:  $1.55 \pm 2.3 \text{ h}$  (mean  $\pm$  standard deviation), spanning the range 0.17 h minimum to 16.0 h maximum for frame C; and  $0.90 \pm 1.3 \text{ h}$ , 0.17 h minimum, and 12.0 h maximum for frame D.

### 3.2. Ripple Wavelength Versus Wave Orbital Excursion

[20] The LTR wavelength distributions are plotted in Figure 8, and the wavelength statistics are listed in Table 3. The mean wavelength was  $\sim 7.6 \text{ cm}$  at both frames, consis-

tent with values reported by Hay and Mudge [2005]. The distribution width, as represented by twice the standard deviation, is about 20% of the mean, or  $\sim 1 \text{ cm}$ .

[21] Figure 9 shows the LTR data in ripple wavelength versus wave orbital diameter space normalized by the median grain diameter, together with the data compiled by Wiberg and Harris [1994]. Here  $d_0$  is defined as the significant wave orbital excursion  $2u_{1/3}/\omega_p$ , where  $u_{1/3}$  is the significant wave orbital velocity and  $\omega_p$  is the angular frequency at the peak in the wave energy spectrum. The LTR data plot in a band parallel to the  $d_0/D_{50}$  axis between  $4.3 \times 10^3$  and  $2.5 \times 10^4$ , which is very similar to the  $3 \times 10^3$  to  $2 \times 10^4$  range of  $d_0/D_{50}$  values reported by Wiberg and Harris [1994, Figure 3a] for anorbital ripples. The mean value of  $\lambda_0/D_{50}$  is 535 at frame C and 524 at frame D, both very close to the value of 535 for anorbital ripples given by

**Table 2.** Mean Hydrodynamic Forcing Parameters for the Automatically Detected Linear Transition Ripple Occurrences at Both Frames<sup>a</sup>

	Frame C	Frame D
$\alpha$ (deg)	$-1.9 \pm 9.6$	$-3.4 \pm 8.2$
$ \alpha $ (deg)	$8.1 \pm 5.4$	$7.2 \pm 5.1$
$u_{rms}$ ( $\text{m s}^{-1}$ )	$0.25 \pm 0.041$	$0.25 \pm 0.039$
$ v_c $ ( $\text{m s}^{-1}$ )	$0.083 \pm 0.072$	$0.059 \pm 0.045$
$u_c$ ( $\text{m s}^{-1}$ )	$-0.067 \pm 0.036$	$-0.038 \pm 0.025$
$u_{IG}$ ( $\text{m s}^{-1}$ )	$0.056 \pm 0.014$	$0.050 \pm 0.012$

<sup>a</sup>The values listed are means  $\pm$  standard deviations;  $u_{IG}$  is the RMS infragravity wave velocity.

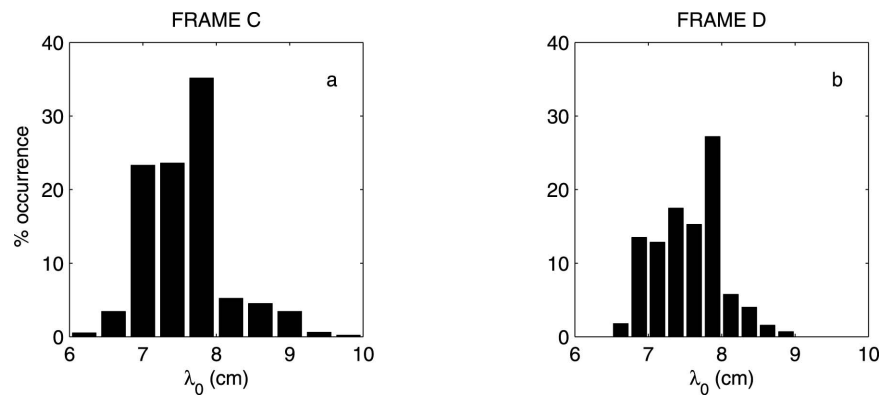


**Figure 8.** Distribution of linear transition ripple wavelengths from the automatic detection record at (a) frame C and (b) frame D. The mean wavelength is 7.6 cm at both frames (see Table 3).

*Wiberg and Harris* [1994, equation (8)]. The number of new data points added to the anorbital region (the box outlined in Figure 9a) is 912, compared to 22 for the data compiled by *Wiberg and Harris* [1994]: 582 of the new points are from frame C and 330 from frame D (both less than the number of LTR images in Table 1 because values for  $d_0$  are available at only 1/2 h intervals). Notably, the SandyDuck97 data indicate that the anorbital range extends to values of  $d_0/D_{50}$  below the lower limit of 5000 given by *Clifton and Dingler* [1984], consistent with the data reported by *Crawford and Hay* [2001] from the 1995 experiment at Queensland Beach, NS.

[22] The ripple wavelengths in Figure 9b are nearly independent of orbital diameter, consistent with the anorbital ripple type defined by *Clifton* [1976] and *Clifton and Dingler* [1984]. Because the observed ripples are also long crested, and because they occur at wave energies immediately below transition to flat bed, they are classified here as Linear Transition Ripples, consistent with the terminology used by *Conley and Inman* [1992] and in subsequent studies [e.g., *Crawford and Hay*, 2001; *Hay and Mudge*, 2005].

[23] There is a slight tendency in Figure 9b for the LTR wavelengths to increase with increasing wave orbital diameter. Since ripple wavelength is expected to be independent of wave orbital diameter for anorbital ripples, one possible explanation for this tendency is that  $D_{50}$  increased with  $d_0$ . Given the width of the sediment size distribution at the two instrument locations [*Hay and Mudge*, 2005], we suggest that the  $\pm 10\%$  observed variation in  $\lambda_0/D_{50}$  could have been due to  $\pm 10\%$  temporal changes in median grain size: that is, to winnowing of fine material from the bed with increasing orbital excursion (equivalent to wave energy, since the wave period was consistently  $9 \pm 2$  s) [*Hay and Mudge*, 2005].

[24] Thus, the LTR results from SandyDuck97 in Figure 9 are in very good agreement with the values of  $\lambda/D_{50}$  and

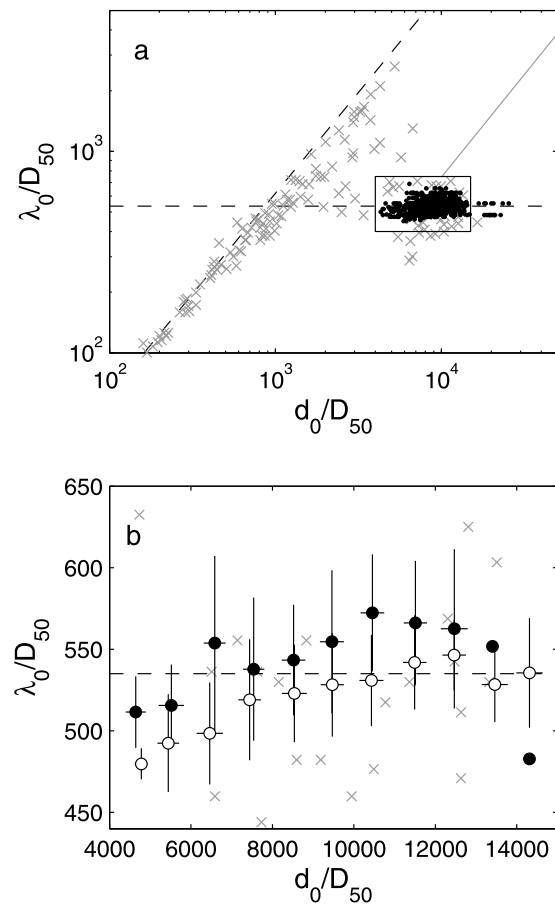


**Figure 9.** (a) Ripple occurrences in orbital diameter versus ripple wavelength space. The LTR data from the present study are indicated by the black dots; the data from *Wiberg and Harris* [1994] for all ripple types are indicated by the grey crosses. The dependencies of orbital-scale and anorbital ripple wavelengths on orbital diameter are indicated by the sloping and horizontal dashed lines, respectively. The sloping solid grey line indicates the nominal behavior of (high sediment transport rate) rolling grain ripples. (b) Close-up of the box outlined in Figure 9a. Solid black and open circles are the averages over intervals of  $10^3$  in  $d_0/D_{50}$  for frame C and D, respectively. The error bars represent  $\pm 1$  standard deviation.

**Table 3.** Wavelength,  $\lambda_0$ ,  $d_0/D_{50}$ , and  $\lambda_0/D_{50}$  for Linear Transition Ripples at Each Frame<sup>a</sup>

	$\lambda_0$ (cm)	$d_0/D_{50}$ ( $\times 10^3$ )	$\lambda_0/D_{50}$
Frame C	$7.6 \pm 0.6$	$9.5 \pm 3.2$	$535 \pm 46$
Frame D	$7.6 \pm 0.5$	$9.3 \pm 2.2$	$524 \pm 33$

<sup>a</sup>Values are means  $\pm$  standard deviations.

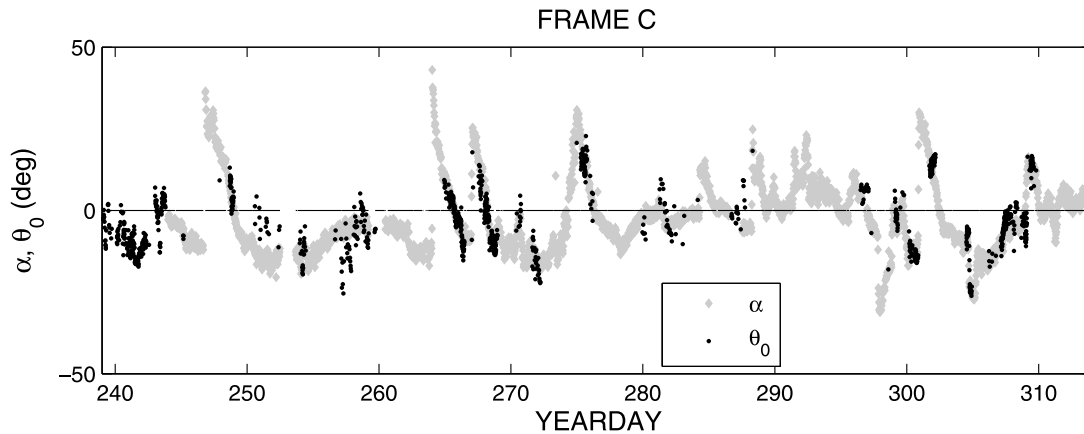


**Figure 10.** Time series of linear transition ripple orientations and incident wave directions for frame C (grey is wave directions,  $\alpha$ ; black is ripple orientations,  $\theta_0$ ).

$d_0/D_{50}$  for anorbital ripple occurrence given by *Wiberg and Harris* [1994]. The *Wiberg and Harris* [1994] values were based on field data. In addition, the LTR wavelength observations from the 1995 Queensland Beach experiment reported by *Crawford and Hay* [2001] are also consistent with the present results. However, the field results are at odds with ripple measurements from recent experiments in large-scale laboratory facilities. *O'Donoghue et al.* [2006] compiled ripple wavelengths from experiments in prototype-scale oscillatory flow and wave flumes and found that, instead of constant wavelength anorbital ripples at high orbital excursions, ripple wavelengths tended to continue to increase more or less in accordance with the orbital ripple relationship. Thus, *O'Donoghue et al.* [2006] concluded that the occurrence of ripples with constant wavelength for values of  $d_0$  beyond the orbital regime “is in general disagreement with the large-scale laboratory data”, and therefore that the “large-scale experimental data casts some doubt on the field data or on *Wiberg and Harris*’ interpretation of the field data”. In contrast, the present observations substantiate clearly and unequivocally the existence of constant wavelength ripples immediately below the flat bed threshold, consistent with the old field data.

[25] Also shown in Figure 9a is a line indicating the nominal behavior of high sediment transport rate rolling grain ripples. This line is based on Figure 4.11 of *Sleath* [1984], in which  $\lambda_0/D_{50}$  is plotted versus  $0.5d_0/D_{50}$  for various values of the wave period parameter. The latter is given by [*Mogridge and Kamphuis*, 1972; *Mogridge et al.*, 1994]

$$\xi = D_{50} / [(s-1)gT_p^2] \quad (3)$$

where  $s$  is the sediment specific gravity,  $g$  the acceleration due to gravity, and  $T_p$  the peak wave period. For the present data set  $\xi \sim 0.1 \times 10^{-6}$ . Of the curves plotted by *Sleath* [1984], one has a comparable value of  $\xi$  ( $\sim 0.2 \times 10^{-6}$ ). This curve levels out at values of  $\lambda_0/D_{50}$  and  $d_0/D_{50}$  corresponding roughly to the observed anorbital range in Figure 9. For values of  $d_0/D_{50} \gtrsim 10^4$ , however, the predicted rolling grain ripple wavelengths exhibit a linear dependence on orbital excursion, as indicated in Figure 9a.

Ripples with wavelengths proportional to orbital excursion have not been observed in the *SandyDuck97* rotary sonar data at high wave energies. Instead, the visual examination of the imagery has indicated that the LTRs are eroded and the bed becomes flat as wave energy increases [*Hay and Mudge*, 2005].

### 3.3. Ripple Orientation Versus Incident Wave Direction

#### 3.3.1. Bulk Statistics

[26] Time series of ripple orientation,  $\theta_0$ , and incident wave direction,  $\alpha$ , are presented in Figure 10 for frame C. The data for frame D (not shown) are very similar [*Maier*, 2008]. Incident sea-and-swell directions when LTRs were present are small on average, typically within  $\pm 10^\circ$  of shore normal. Maximum sea-and-swell directions for instances of LTRs are up to  $\pm 30^\circ$ . Figure 11 shows scatterplots of  $\theta_0$  versus  $\alpha$  for both frames. The ripple orientations correlate well with wave direction (frame C,  $r^2 = 0.74$ ; frame D,  $r^2 = 0.46$ ).

[27] Figure 12 shows the distributions of the difference between wave and ripple directions,  $|\alpha - \theta_0|$  and  $FWHM_\theta$  from the Radon transform method. Note the breadth of the  $FWHM_\theta$  distribution, indicating that much of the scatter in the ripple wave direction relationship may be attributable to uncertainties in the ripple orientation, together with the possible errors in the wave directions, estimated to be about  $\pm 5^\circ$ . The main point to be taken from Figure 12 is that  $\sim 60\%$  of ripple orientations differ from the wave direction by less than  $5^\circ$ , and more than  $90\%$  by less than  $10^\circ$ .

#### 3.3.2. Time Variations in Ripple Orientation

[28] Ripple orientations frequently followed the incident wave direction closely: for example, YD 249, 265, 268 and 275 (Figure 10). Typically, these instances were associated with storm decay, and were characterized by  $u_{rms}$  values greater than  $0.22 \text{ m s}^{-1}$ , weak mean currents ( $|u_c|, |v_c| \leq 0.1 \text{ m s}^{-1}$ ), and slowly changing wave direction.

[29] In several instances, however, the wave direction changed abruptly. Two such events are shown in Figure 13. Each exhibits a change in wave direction of 10 to  $20^\circ$  over 1 to 3 h. In each case, the ripple orientation angles are aligned with the wave direction both before and after the wave direction change, but ripple reorientation lags behind

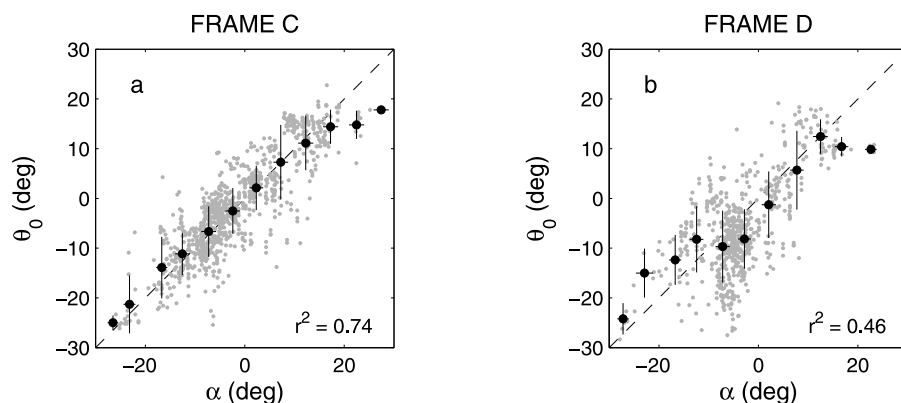


**Figure 11.** Scatterplots of linear transition ripple orientation,  $\theta_0$ , versus incident wave direction,  $\alpha$ , for (a) frame C and (b) frame D. The  $r^2$  values are based on the individual data points (grey); the error bars represent  $\pm 1$  standard deviation from the averages (solid black circles) at  $5^\circ$  intervals in  $\alpha$ .

the waves by 1 to 2 h. The direction change in Figure 13a occurred just before a storm event, and was accompanied by an increase in  $u_{rms}$  from 0.17 to 0.30  $\text{m s}^{-1}$ . As Figure 13 indicates, only when  $u_{rms}$  increased from 0.20 to 0.25  $\text{m s}^{-1}$  did the ripples begin to change direction. The second event (Figure 13c) also occurred before a storm and again, the change in ripple orientation began when  $u_{rms}$  exceeded 0.25  $\text{m s}^{-1}$ .

[30] Figure 14 shows a sequence of wave directional spectra from the EM flowmeter data for the period spanning the shifts in wave direction and ripple orientation in Figure 13a. The time origin for the different plots in Figure 13 is YD 304.7028, the time when the ripple orientation began to change (the vertical line in Figure 13a). Initially, about half an hour before the ripples start to shift, the spectrum was bimodal in frequency. Subsequently these lobes merged as the wave direction changed and wave energy built sharply. Other than this increase in wave energy (consistent with Figure 13b), there is no feature of the directional spectra that seems obviously related to the reorientation of the ripples. Thus, these results indicate that only when  $u_{rms}$  exceeded 0.25  $\text{m s}^{-1}$  were the ripples able to reorient to the new wave direction.

[31] Subimages of the seabed at four different times during the YD304 reorientation event are shown in Figure 15. To illustrate how these ripples changed orienta-

tion, two subimages at an intermediate stage during the reorientation process, one from each of the two events, are presented in Figure 16 together with corresponding sketches of the ripple crestlines. The sketches indicate that, during adjustment, the ripple crests broke up into line segments and bifurcations appeared at irregular spacings. Remnants of crest segments that had not yet turned are visible. Bridges between crests are present, sometimes resulting in diamond shaped patterns. The bridging features are aligned at steeper angles than the final crest orientation. Similar features have been observed during reorientation of orbital ripples [Traykovski *et al.*, 1999]. A difference in the anorbital case, likely related to the wave orbital excursions being large compared to the equilibrium ripple wavelength, is that individual bridging features can intersect several ripple crests aligned in the original orientation. Nevertheless, as for orbital ripples, LTR crests reorient themselves in a piecewise manner. As a result, and as Figure 16 indicates, the reorientation process is accompanied by the creation of multiple defects in the ripple pattern. Presumably, if the wave forcing persists in the same new direction while maintaining sufficient energy, many of these defects would eventually be annealed out, leaving a nearly defect-free pattern, as in Figure 5.

[32] Table 4 lists  $\theta_0$ ,  $FWHM_\theta$ , and  $\lambda_0$  for the two events. There is a tendency for  $FWHM_\theta$  to increase and reach a

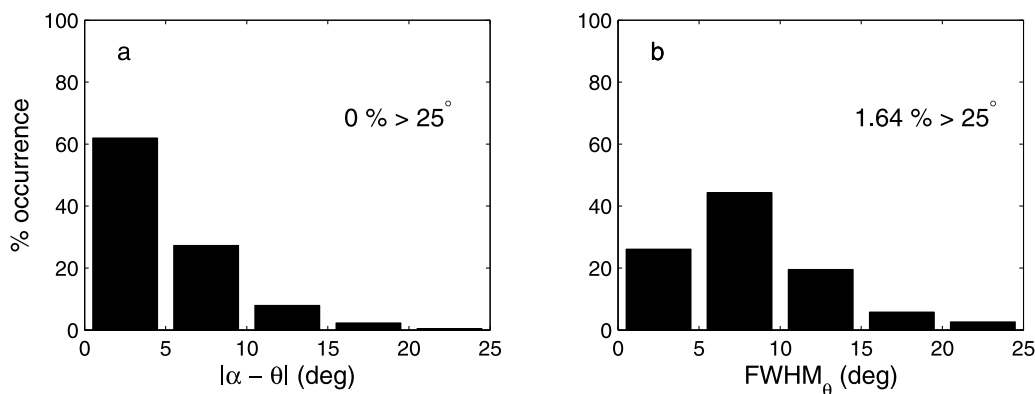


**Figure 12.** Distributions of (a) the ripple wave offset,  $|\alpha - \theta|$ , and (b) the error estimate of the Radon method, full width at half maximum ( $FWHM_\theta$ ), in % occurrence for both frames combined. The  $>25^\circ$  numbers indicate the % occurrences above  $25^\circ$  not shown in the histograms.

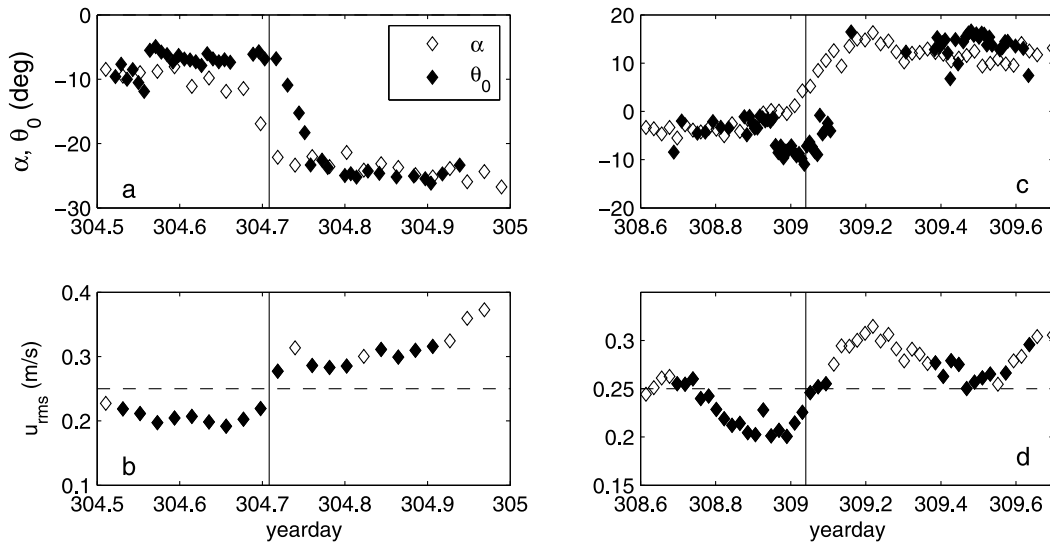


**Figure 13.** (a and c) Ripple orientation (black diamonds) and wave direction (open diamonds) for two events exhibiting rapid changes in wave direction. (b and d) The corresponding  $u_{rms}$  values, with linear transition ripple occurrences indicated in black. The dashed lines indicate  $u_{rms} = 0.25 \text{ m s}^{-1}$ , the mean value of  $u_{rms}$  for linear transition ripple occurrence. The vertical lines indicate the time when the ripples start to change orientation. Note that in both cases this time corresponds to  $u_{rms}$  rising above  $0.25 \text{ m s}^{-1}$ .

maximum value during adjustment. We attribute the increase in  $FWHM_{\theta}$  to the piecewise rotation of crest segments, and resulting increase in the directional spread in the Radon transform variance. The maximum in  $FWHM_{\theta}$  is attributed to a maximum in the number of defects since, as indicated above, the number of defects increases initially due to the piecewise rotation of crest segments, and then decreases as defects are annealed out under the persistent

action of waves from the new direction. A tendency for  $\lambda_0$  to increase is also indicated in Table 4. We suggest that this increase could be due to winnowing.

#### 4. Discussion

##### 4.1. Ripple Response Time

[33] *Traykovski et al.* [1999] found that orbital-scale ripples are generally aligned with the waves forming them

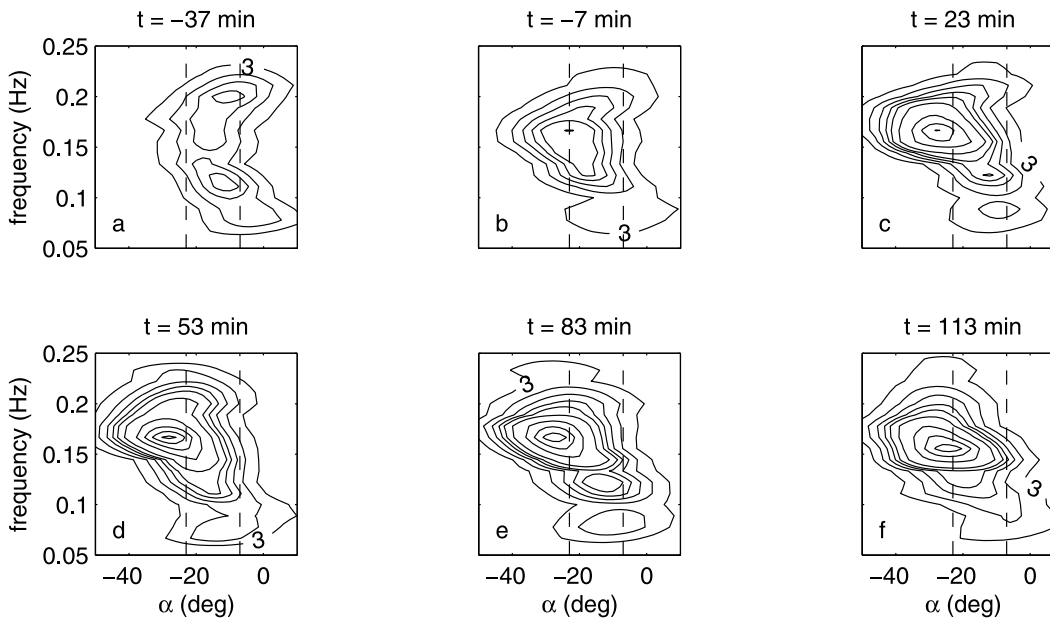


**Figure 14.** Wave directional spectra during the abrupt change in wave direction on YD 304 shown in Figure 13a. The time origin,  $t = 0$ , corresponds to YD 304.7028, the time when the ripples begin to change (dashed line in Figure 13a). The dashed lines indicate the ripple orientations before and after the adjustment ( $-7^{\circ}$  and  $-23^{\circ}$ ). Contours start at  $3 \times 10^{-3} \text{ m}^2 \text{ s}^{-2} \text{ Hz}^{-1} \text{ deg}^{-1}$ . The contour interval is  $2 \times 10^{-3} \text{ m}^2 \text{ s}^{-2} \text{ Hz}^{-1} \text{ deg}^{-1}$  for the first four contours, and  $10 \times 10^{-3} \text{ m}^2 \text{ s}^{-2} \text{ Hz}^{-1} \text{ deg}^{-1}$  thereafter.

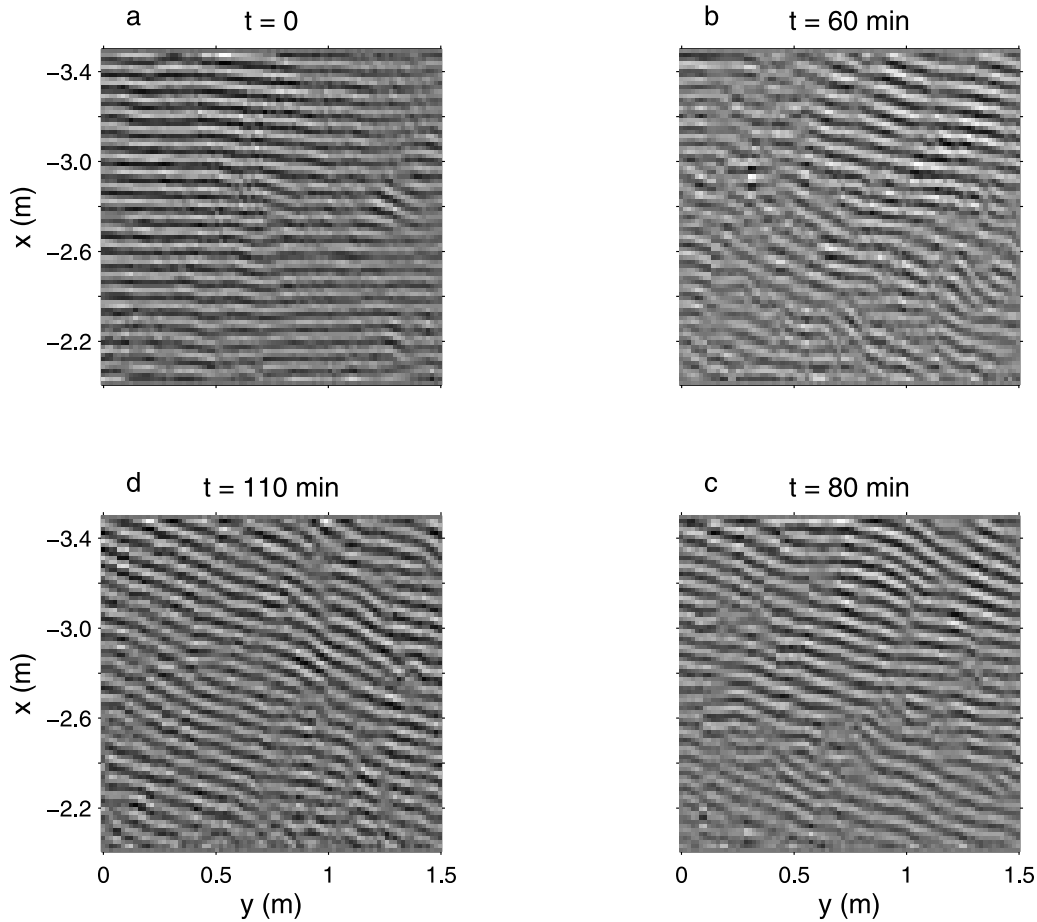


**Figure 15.** Sequence of images highlighting the abrupt change in ripple orientation in Figure 13a starting at YD 304.7028. Time increases clockwise from the top left.  $\theta_0$  changes from  $-2^\circ$  at  $t = 0$  to  $-18^\circ$  after 110 min.

except during times of low wave energy when an offset between ripple orientation and wave direction can occur. This offset was attributed to hysteresis, whereby ripples formed during a storm event are unable to remain in equilibrium with the forcing when wave energies drop off too quickly, relative to the ripple response time. We have presented evidence for a related phenomenon for anorbital ripples, for sufficiently rapid changes in wave direction, but during times of increasing wave energy. This observation is at variance with the hypothesis put forward in the Introduction, that anorbital ripples, being small and existing at high wave energies (i.e., immediately below the flat bed transition), should respond quickly. Thus, an examination of likely LTR response times is in order.

[34] In his model of orbital-scale ripple adjustment, *Traykovski* [2007] proposed that the ripple response time,  $T_R$ , can be estimated as the ratio of the volume of sediment in the ripple to the volume rate of sediment transport by bed load:

$$T_R = (1 - n) \frac{\eta_o \lambda_o}{2Q_b} \quad (4)$$

where  $n$  is the sediment porosity,  $\eta_o$  the ripple height, and  $Q_b$  the bed load transport across the ripple crest during a

half cycle. Using the bed load formula proposed by *Meyer-Peter and Müller* [1948],  $Q_b$  can be written as

$$Q_b = \frac{A}{(s-1)g} \left( \frac{\tau_b}{\rho} \right)^{3/2} \quad (5)$$

where  $A$  is a constant. In writing equation (5), it has been assumed that the bottom stress,  $\tau_b$ , is much greater than the critical stress for grain movement, an appropriate assumption here given that LTRs occur just below the flat bed threshold. While there is not unanimity on the most appropriate formula for wave-driven bed load transport [see, e.g., *Nielsen*, 1992; *Fredsoe and Deigaard*, 1992], the analysis by *Ribberink* [1998] of results from laboratory experiments with steady, oscillatory and combined flows yielded an overall best fit value of 1.65 for the exponent, close enough to 1.5 for the purpose of estimating the adjustment time scale, and a value of 11 for  $A$ . (Note that in order to obtain a universal value for the exponent, *Ribberink* [1998] used different grain roughnesses for oscillatory and steady flows at Shields parameters below unity.)

[35] The Shields parameter is given by

$$\vartheta = \frac{f'_w u_b^2}{2(s-1)gD_{50}} \quad (6)$$

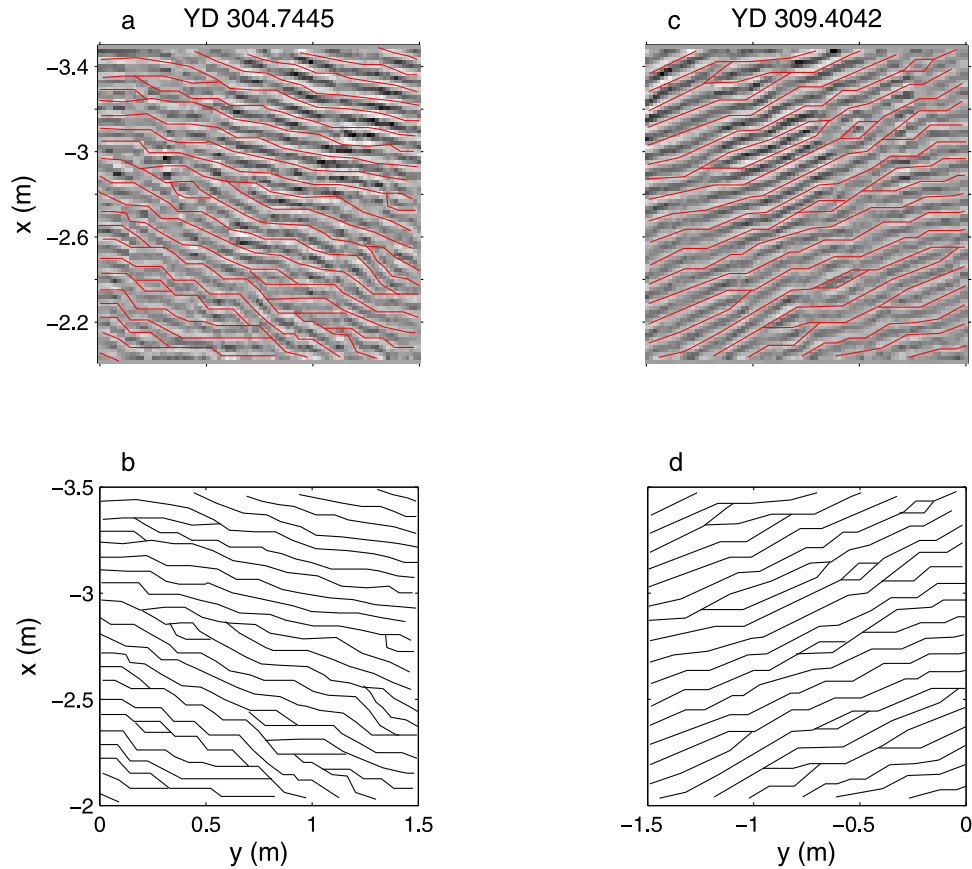


**Figure 16.** Illustration of the segmented, or stepwise, orientation changes along ripple crests during LTR adjustment to rapid changes in wave direction. The data are from the two events in Figure 13. (a and c) Grey-scale subimages with crestlines superposed (red). (b and d) Crestlines only.

where  $f'_w$  is the wave friction factor for fixed grain roughness [Nielsen, 1992]. Using Swart's expression for  $f'_w$  [Swart, 1974; Nielsen, 1992],  $u_b = u_{1/3} = 0.5 \text{ m s}^{-1}$ ,  $T_p = 9 \text{ s}$  [Hay and Mudge, 2005], and either  $D_{50}$  or  $2.5D_{50}$  for the physical roughness yields values of  $f'_w$  of 0.007 and 0.008, and grain roughness Shields parameter estimates of 0.37 and 0.45. These values are an order of magnitude greater than the critical value for grain movement, 0.05 [Nielsen, 1992].

[36] The bottom stress is given by

$$\tau_b = \rho f_w u_b^2 / 2 \quad (7)$$

where  $f_w$  is the wave friction factor, and  $u_b$  is a representative near-bed wave orbital velocity. Smyth and Hay [2002] and Newgard and Hay [2007] have compared observed estimates of  $f_w$  based on near-bed turbulence measurements to existing semiempirical formulae, as a function of bed state during SandyDuck97. From Newgard and Hay, [2007, Figure 13]  $f_w \sim 0.01$  for  $\vartheta \sim 0.4$ , comparable to the fixed grain roughness values for  $f'_w$  and  $\vartheta$  given above.

[37] The above equations can be combined to obtain a relation for the nondimensional bed load transport,  $\Phi_b = Q_b / [(s - 1)gD_{50}^3]^{-1/2}$ :

$$\Phi_b = A\vartheta^{3/2} \quad (8)$$

This equation comes up later.

[38] Returning to equation (5) and substituting  $n \sim 0.5$ ,  $A \sim 10$ ,  $s = 2.6$ ,  $u_b \sim 0.5 \text{ m s}^{-1}$ ,  $f_w \sim 0.01$ , one obtains  $Q_b = 2.7 \times 10^{-5} \text{ m}^2 \text{ s}^{-1}$ . Substituting this value of  $Q_b$  in equation (4), together with  $\lambda_o = 0.075 \text{ m}$  and  $\eta_o = 0.003 \text{ m}$  [Crawford and Hay, 2001], yields  $T_R \sim 2 \text{ s}$ . A ripple adjustment time scale on the order of a few seconds is consistent with the previous observations, cited in the Introduction, of LTRs being erased on wave period time scales. However, a time scale on the order of seconds contrasts sharply with the observations presented here of an O(1 h) time scale for LTR reorientation. The  $T_R$  estimate is sensitive to the choice of  $u_b$ . If, for example, we let  $u_b = 2u_{rms} = 0.4 \text{ m s}^{-1}$ , a representative value immediately before the waves started to change direction (Figures 13b and 13d),  $T_R$  increases to 4 s. Adjustments in

**Table 4.** Ripple Orientation, Error Estimate  $FWHM_\theta$ , and Ripple Wavelength During the Two Events in Figure 13

	$t$ (min)	$\theta_0$ (deg)	$FWHM_\theta$ (deg)	$\lambda_0$ (cm)
Event 1	0	-2	7	7.3
	60	-10	6	9.5
	80	-19	9	8.0
	110	-18	8	7.8
Event 2	0	-4	5	8.0
	1.3	2	5	8.0
	2.7	23	16	9.0
	8.5	18	13	10.0

the other parameters could certainly change this estimate by additional factors of 2, so an overall increase by a factor of 10 (to 20 s say) may be possible. Note, however, that the value chosen for  $f_w$  is at the bottom end of the likely range, and could not be reduced by more than 50% without falling below the fixed grain roughness value. Note as well that, while we have used the value for LTR ripple height obtained by *Crawford and Hay* [2001] at a different field site, their values of several mm are consistent with those obtained by *Dingler and Inman* [1977] at yet another location. Furthermore, similar values have also been obtained from an analysis of the rotary pencil beam sonar data from the SandyDuck97 experiment, yielding best estimates of the minimum and maximum possible values for  $\eta_0$  of  $1.5 \pm 2$  mm and  $12.3 \pm 2.6$  mm, respectively. While these values are best regarded as preliminary (the analysis involves a correction for the finite beam width of the pencil beam sonars which is being tested still), they are nonetheless consistent with the  $\leq 0.1$  steepnesses expected for anorbital ripples, and indicate that it is unlikely that  $\eta_0$  greatly exceeded 7 or 8 mm. Thus, adjusting the various parameters within reasonable bounds would not lead to an increase in  $T_R$  by several orders of magnitude, indicating that either (1) the time scale given by equation (4) is incorrect or (2) some additional physical process must be involved which has the effect of decreasing  $Q_b$ . We explore each of these possibilities in the next two sections.

#### 4.2. Laboratory Measurements of Ripple Response Times

[39] *Doucette and O'Donoghue* [2006] (DO) carried out a series of large-scale laboratory experiments on the temporal development of ripples on a bed of 440  $\mu\text{m}$  median diameter sand under the action of both regular and irregular oscillatory flows. The oscillation periods ranged from 2 to 12.5 s, and the orbital excursions from 0.24 to 2.0 m. At equilibrium, the ripples were orbital scale, with  $\lambda \sim 0.45d$ . The equilibration time,  $T_e$ , was defined as the time for the ripple height to reach 95% of its equilibrium value. *Doucette and O'Donoghue* [2006] obtained an empirical relationship between  $T_e$  and the mobility parameter  $\Psi = u_b^2/[(s-1)gD_{50}]$ :

$$n_e = \frac{T_e}{T_p} = \exp[-0.036\Psi + 7.44] \quad (9)$$

where  $n_e$  is the number of oscillation cycles corresponding to the response time. *Soulsby and Whitehead* [2005] (SW) obtained a second empirical fit to these same data. Their fit, which is forced to tend to infinity as  $\Psi$  tends to zero, can be written as

$$n_e = \left[ \frac{21700 + \Psi^{1.07}}{2.996\Psi^{1.07}} \right] \ln(20) \quad (10)$$

where the  $\ln(20)$  factor arises because *Soulsby and Whitehead* [2005] computed the  $e$ -folding time.

[40] While neither of the empirical expressions above appear on casual inspection to be compatible with equation (4), we now proceed to demonstrate that they

are. As a first indicator, and noting that  $\vartheta = f_w\Psi/2$  and making use of equation (8), we have plotted  $n_e/\Psi^{3/2}$  in Figure 17a for the range of  $\Psi$  values spanned by the DO experiments. Note that the predicted response times when normalized by  $\Psi^{3/2}$  vary by less than a factor of 3.

[41]  $Q_b$  was computed for the DO experiments using equation (5) and the *Swart* [1974] formula for  $f_w'$  with  $2D_{50}$  for the roughness, and  $u_b$  from the values of  $\Psi$  given by *Doucette and O'Donoghue's* [2006] Table 1. The resulting estimates are plotted in Figure 17b, and are  $\leq 5 \times 10^{-5} \text{ m}^2\text{s}^{-1}$ . For comparison, the values of net bed load transport obtained by *Doucette and O'Donoghue* [2006] from ripple migration rates are an order of magnitude smaller, so the estimates for the average bed load transport in a half cycle in Figure 17b would appear to be reasonable. The values of  $T_R$  obtained using these  $Q_b$  estimates and equation (4) are plotted against the observed  $T_e$  values in Figure 17c. The predicted and observed values are of the same order, and the predictions account for 50% of the variance in the observations. However, we are most interested in high transport conditions (short response times), and have therefore plotted the response rates in Figure 17d. At first glance there is much more scatter among the data points plotted this way. However, if we select those points which correspond to high sediment transport ( $\Psi > 25$ ), the data are much less scattered, and are clustered about the 1:1 line.

[42] Thus, Figure 17 indicates that the DO experimental results are consistent with the response time given by equation (4), within a factor of 2 or so, at least for the higher values of the mobility parameter (for comparison, the value of  $\Psi$  for the present results, based on  $u_{1/3}$ , is  $\sim 80$ ). Considering that equation (4) is based on a physical argument (or one might also say, a dimensional argument) rather than an empirical fit, this degree of consistency is encouraging. Furthermore, the above discussion indicates that ripple response times can be estimated from the ripple volume and the bed load transport rate computed using the *Meyer-Peter and Müller* [1948] formula and the grain roughness to estimate the bed shear stress. Consequently, based on this comparison with laboratory results, the time scale for LTR adjustment is expected to be of the same order as the wave period, consistent with the previously cited observations of these ripples being created and destroyed on wave period and wave group time scales.

[43] Laboratory experiments on the temporal development of sand ripples have also been carried out by *Smith and Sleath* [2005] and *Davis et al.* [2004]. The mobility numbers in the latter experiments were less than 10, and so are not discussed further here. *Smith and Sleath's* [2005] experiments, for orbital-scale ripples in 140  $\mu\text{m}$  median diameter sand, reached  $\Psi$  values as high as 90. The adjustment times were measured from an initially rippled state at a different oscillation period, and so are not as readily compared to  $T_R$  as the DO results. Nevertheless, calculating  $f_w'$  and  $Q_b$  as above, and using *Smith and Sleath's* [2005] final ripple heights and wavelengths to estimate ripple volume, we computed the number of cycles to reach 80% of the final height,  $\ln(5)T_R/T_f$ , where  $T_f$  is the oscillation period for ripple development following the initial state. A plot (not shown) of computed against

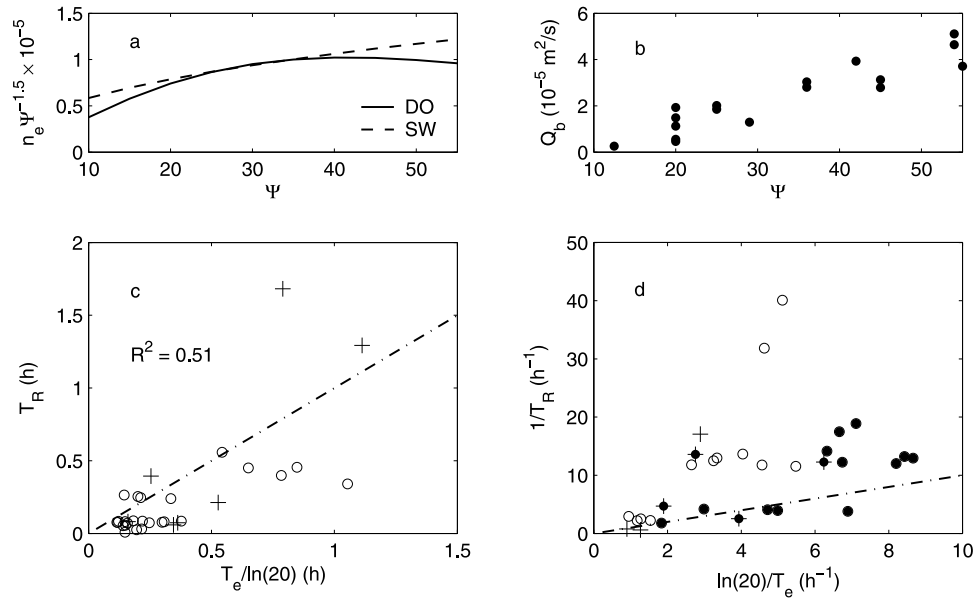


**Figure 17.** (a) Number of wave cycles,  $n_e$ , for ripples to reach equilibrium according to *Doucette and O'Donoghue* [2006] (DO) and *Soulsby and Whitehead* [2005] (SW) divided by  $\Psi^{3/2}$ . Note that the variation in the ordinate is only a factor of 2 over the range of  $\Psi$  values spanned by the DO experiments. (b) Predicted bed load transport rates for the DO experiments. (c) Ripple response times for the DO experiments predicted using equation (4),  $T_R$ , compared to the observed response times,  $T_e$ . Also shown are the  $R^2$  values between the measured  $T_e$  values and the predictions,  $T_R$ . The dashed-dotted line represents 1:1 correspondence between  $T_e/\ln(20)$  and  $T_R$ . Open circles and plus signs indicate the results for regular and irregular waves, respectively. (d) The same data as in Figure 17c, but plotted as the response rate to reveal the behavior at faster response times. The black dots indicate the values for  $\Psi > 25$  (i.e., the higher sediment transport rates).

observed times indicates that the observed values are 7 to 80 times longer than the predictions, and about 20 times longer on average. Response times 20 times longer than given by equation (4) would give 40 s for the LTR response time, which is still comparable to wave group time scales. Finally, based on their laboratory experiments, *Voropayev et al.* [1999] obtained a formula for ripple  $e$ -folding time which can be written as  $n_e = 2500/[2\pi\Psi^{1/2}]$ , and which also compared well with the later experiments by *Testik et al.* [2005]. For  $\Psi \sim 80$ , this formula gives ca. 45 cycles corresponding to an adjustment time of 400 s. However, *Voropayev et al.* [1999] carried out only one experiment at a high  $\Psi$  value (39), the remainder being below 15, and  $\Psi$  was 16 or less in the *Testik et al.* [2005] experiments.

### 4.3. Bypassing

[44] A potential mechanism for reconciling the several orders of magnitude difference between the observed and predicted time scales for LTR reorientation is sediment bypassing. The bypassing concept dates at least as far back as *Hubbell* [1964], who argued that bed load grains hopping over one dune or ripple to the next would bias the bed load transport rate estimated from bed form migration measurements. *Rubin and Hunter* [1982] identify the bypassing component of the total transport as the “throughgoing” transport, and, for the case of ripples on the stoss side of aeolian dunes, state that “much of the bed load transport over aeolian ripples bypasses the ripples”.

[45] Kinematically, ripple development arises from the divergence of the sediment transport. Thus,

$$\frac{\partial \eta}{\partial t} = -\frac{\nabla \cdot \vec{Q}}{1-n} \quad (11)$$

Here  $\eta$  is the bed elevation,  $n$  the porosity of the bed, and  $\nabla \cdot = \partial/\partial x \hat{i} + \partial/\partial y \hat{j}$  is the two-dimensional divergence operator,  $\hat{i}$  and  $\hat{j}$  being unit vectors. For the case of a sinusoidal ripple profile of the form  $\eta = a_0 \exp[ik_0(x - ct)]$  and  $Q$  phase locked to the ripple profile such that transport is high over the crests and low in the troughs, substitution in equation (11) yields the usual expression for the ripple migration speed,  $c$ :

$$c = \frac{Q_0}{(1-n)a_0} \quad (12)$$

In oscillatory flow,  $Q_0$  is replaced by  $Q_{net}$ , the net transport over a cycle. Thus, an equilibrium is kinematically possible in which ripples of constant wavelength and amplitude are either stationary ( $Q_{net} = 0$ ) or migrating ( $Q_{net} \neq 0$ ).

[46] Recall, however, the assumption that  $Q$  is phase locked to the ripple profile. Clearly, one can add any spatially uniform transport without changing the divergence. It is also clear that, in principle, the spatial structure of the cycle-averaged transport could involve other wave

numbers. Now, return to the two-dimensional case, and allow the direction of the wave forcing to change. The ripples obviously cannot wheel around intact, as this would require some specific center of rotation and extremely high migration speeds at great distances from this center, neither of which is physically realistic. Instead, the directional adjustment must occur in a piecewise fashion, as previously proposed by *Traykovski et al.* [1999], and as indicated in Figure 16. Specifically, only a portion of the transport divergence would contribute to the ripple field with wave vector  $k_0$  aligned with the new direction of the incident surface gravity waves, until the amplitudes of all other wave vectors created by the piecewise adjustment were erased.

[47] We designate the bypassing associated with spatially uniform bed load transport as Type A, and that associated with divergence at different wave vectors in the 2-D case, as Type B. For ripples reorienting in response to changing wave direction, Type B bypassing would seem likely, and possibly even necessary, given the creation of bed elevation variance at different spatial wave vectors (which is implicit in Figure 16). Finally, we suggest that the many obliquely oriented line segments in the adjusting ripple pattern (Figures 15 and 16) could result in increased sediment suspension, and thus a third bypassing mechanism, Type C, via the suspended load.

[48] In order for the value of  $T_R$  to increase from  $O(10\text{ s})$  to  $O(10^3\text{ s})$ , only 1% of the bed load transport can be associated with the volume of the LTRs, given equation (4). The remaining 99% of the transport would have to be diverted to the creation of bed features at other spatial scales, or into the suspension, or some combination of both. Whether this is in fact the mechanism responsible for the delayed orientation adjustment indicated in Figure 13 cannot be determined from the present data set. However, the mechanism is certainly testable in principle, and thus we present it here as an hypothesis, to be tested once suitable new sediment dynamics measurement technologies become available.

#### 4.4. Qualifying Remarks

[49] For most of the LTR occurrences in the SandyDuck97 data set, changes in wave direction were relatively slow, and a delay in the ripple orientation response of  $O(1\text{ h})$  to these slow changes is not discernable in the data. The slowly changing wave directions tended to be associated with storm wave decay and interstorm intervals. The abrupt changes in direction discussed above occurred during storm wave growth. While we have presented only two examples of the response of ripple orientation to abrupt changes in wave direction, these examples are from the onset of 2 of the 12 storms in the record. Of the remaining 10 storms, LTRs either did not occur or appeared only briefly in 5 cases (see Figure 7a), or similarly abrupt changes in wave direction did not occur. Thus, depending upon the location, these results indicate that months long data sets can be required to capture the response to even a few suitably rapid changes in wave direction.

[50] While not presented here, we have compared the LTR migration rates in the SandyDuck97 data to rates computed using equation (12) and the *Meyer-Peter and Müller* [1948] relation for  $Q_b$  [Maier, 2008]. Although there is considerable scatter in the data, the observed and com-

puted migration rates are of the same order, indicating that, once aligned with the waves, bypassing must be much reduced compared to the out of equilibrium conditions associated with active reorientation through large angles, if our bypassing hypothesis is correct.

[51] In a recent paper, *Huntley et al.* [2008] present results from numerical experiments in which the response time of sorted bed forms (i.e., bed forms associated with spatial segregation of a bimodal grain size distribution) decreases with increasing defect density. There are possible parallels with the present investigation. For example, *Huntley et al.* [2008] conclude that “well-established, long-crested bed forms with low defect density are strong inhibitors of changes in bed form characteristics”. One of the properties of LTRs is that they are long crested, and our results also indicate that LTRs are persistent as long as wave energy remains in the appropriate range. Also, we have argued that the creation of bridging elements between the crests of the original ripples is necessary for rotational adjustment, and have presented evidence for their occurrence. These bridging elements can be regarded as a particular type of defect. Thus, an increase in defect density is a necessary part of the reorientation process, and a possible interpretation of our results in the context of the *Huntley et al.* [2008] study is that rotational adjustment is delayed until the defect density is sufficiently high. We agree with this interpretation, but suggest that it does not go far enough, because the defects have to be created. Hence, we argue that creation of the bridging elements represents a transport divergence different from that maintaining the original ripples (i.e., bypassing).

[52] We have searched the rotary sonar imagery from SandyDuck97 for unambiguous indications of LTRs being created or destroyed on wave period time scales, without success. The approach taken thus far has been to examine each of the five consecutive  $360^\circ$  scans (from which each rotary image is constructed) [Hay and Mudge, 2005] for LTR (dis)appearance. Each scan took  $\sim 30\text{ s}$  (i.e.,  $\sim 3$  wave periods) to acquire, and started from the offshore-directed azimuth. A mismatch at this azimuth, such as ripples present on one side and absent on the other, was the sought for unambiguous indicator. The search was restricted to LTR occurrences at higher wave energies. No instances of mismatch were found. *Hanes et al.* [2001] do report “flattening and reforming” of short wavelength ripples (their SWRs) on wave period and wave group time scales in their observations, which were also acquired during SandyDuck97 but farther offshore in ca. 4 m water depth, with a 5 MHz acoustic line array. Their SWR wavelength distribution spanned a 2 to 20 cm range, and was bimodal with one peak at 19 cm and one at 8 cm wavelength: the latter peak likely corresponds to the LTRs discussed here. However, *Hanes et al.* [2001] do not claim that ripples were created or destroyed, stating instead that: “most of our observations after flattening by wave groups indicate that the new ripple crests are coincident with the old. We suggest this is an indication that the seabed was not completely flattened but that *undetectable* SWR were still present.” This statement (with our italics) is compatible with our findings. However, both *Dingler and Inman* [1977], using a 4.5 MHz mechanically translated sonar, and *Conley and Inman* [1992], using video, observed LTRs being either

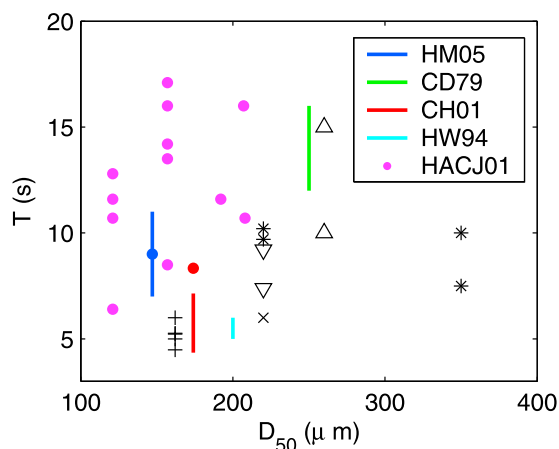


**Figure 18.** Wave period and median grain size for laboratory experiments (black), in which anorbital ripples were expected to occur but were not observed, and field experiments (color) in which anorbital ripples were observed. The laboratory results are those cited by *O'Donoghue et al.* [2006] for  $d_0/D_{50} > 5587$ , using the same symbols as in their Figure 2. The field data are from *Hay and Mudge* [2005] (HM05), *Cacchione and Drake* [1979] (CD79, see also *Wiberg and Harris* [1994]), *Crawford and Hay* [2001] (CH01), *Hay and Wilson* [1994] (HW04), and *Hanes et al.* [2001] (HACJ01).

created or destroyed from one wave to the next. *Dingler and Inman* [1977] state, with respect to their Figure 9, that “This series of bed profiles shows that in fine sand the bed responds rapidly to intense flow and a bed can be flattened and rerippled in a time equivalent to a few wave periods”. D. Conley (personal communication, 2009) has observed LTR (dis)appearance after the passage of individual waves many times visually. Thus, the phenomenon appears to be real enough, so the question is partly one of (system dependent) ripple detection, and partly the specific properties of the forcing leading to its occurrence.

#### 4.5. Field Versus Laboratory Measurements

[53] We now return to the fact that anorbital ripples were not observed in the laboratory experiments summarized by *O'Donoghue et al.* [2006]. The question arises as to whether these experiments were carried out for a region of the relevant parameter space different from the region occupied by the field observations, and from which anorbital ripples are excluded. For example, wave period represents one possibility, as wave periods encountered in the field tend to be longer than the values achievable in laboratory conditions. Wave period is plotted against grain size in Figure 18. The points in black are the laboratory results from *O'Donoghue et al.* [2006] for  $d_0/D_{50} > 5587$ , which they chose for the lower limit of the anorbital range. The points in color are the values from different field experiments corresponding to anorbital ripple occurrences. While the data do exhibit the expected tendency for wave periods to be longer in the field, Figure 18 clearly demonstrates that the field occurrences of anorbital ripples overlap the laboratory nonoccurrences. Thus, the data indicate that some cause other than a particular range of wave periods or grain

sizes (i.e., settling velocities) must have been responsible for the absence of anorbital ripples in these laboratory experiments.

[54] Finally, the results in Figure 9 indicate a value  $d_0/D_{50}$  closer to 4000 than the 5587 value given by *O'Donoghue et al.* [2006] for the lower limit of the anorbital range. Thus, the disagreement between the laboratory and field results is made more serious by the present field data. Furthermore, *O'Donoghue et al.* [2006] use  $d_0 = 2\sqrt{2}u_{rms}/\omega$ , whereas here  $d_0 = 2u_{1/3}/\omega = 4u_{rms}/\omega$ . Thus, it could be argued that their irregular wave results should be plotted at 40% higher values of  $d_0/D_{50}$  to be comparable to Figure 9, increasing the magnitude of the discrepancy further still.

## 5. Summary and Conclusions

[55] The orientation of linear transition ripples during SandyDuck97 is investigated using bed state data from rotary fan beam images and wave data from electromagnetic (EM) flowmeters at 2 locations in  $\sim 3$  m water depth. The data extend over more than 70 days and include 12 major storm events. A method based on the azimuthal variation in the radial spectrum of acoustic backscatter from the seabed was developed to detect LTRs in the sonar record automatically. Ripple orientations, determined from the acoustic images via the Radon transform, were compared to incident wave directions obtained from the EM flowmeter measurements. Probable LTR response times were estimated, and compared to published laboratory measurements for orbital-scale ripples. We draw the following conclusions:

[56] 1. The LTRs observed here are anorbital ripples, in the dual sense that their wavelengths are both much less than, and independent of, the wave orbital excursion. They are not rolling grain ripples, in the sense that the wavelengths of rolling grain ripples are expected to vary linearly with orbital excursion.

[57] 2. A weak dependence of  $\lambda_0$  on  $d_0$  is observed which we suggest could arise from  $O(10\%)$  changes in the  $D_{50}$  of the bed sediments due to winnowing out the finer-grained material as wave energy increased.

[58] 3. The majority (97%) of LTRs occurred for orbital excursions in the range  $4000 \lesssim d_0/D_{50} \lesssim 15000$ . The data indicate a rather sharp cutoff at the lower limit (i.e., no occurrences below  $d_0/D_{50} = 4300$ ), and a more gradual cutoff at the upper limit (i.e., occurrences extending up to  $d_0/D_{50} \sim 25,000$ ).

[59] 4. The observed LTR wavelengths and range of wave orbital diameters over which LTRs occurred during SandyDuck97 are in very good agreement with those expected on the basis of the limits given by *Wiberg and Harris* [1994]. This result contrasts sharply with results from large-scale laboratory facilities summarized by *O'Donoghue et al.* [2006]. We conclude that there is a major, and as yet unresolved, discrepancy between these laboratory experiments and field measurements in the anorbital ripple region.

[60] 5. On average LTR orientations were aligned with the incident waves: that is, with ripple crests perpendicular to the incident wave direction. This result is complementary to field studies of orbital-scale sand ripple orientation [*Traykovski et al.*, 1999; *Smyth and Li*, 2005], which were found to be generally aligned with the wave direction.

[61] 6. LTR reorientation occurs stepwise along the crests, resulting in the introduction of a high spatial density of defects and a multiplicity of new spatial scales in the ripple pattern.

[62] 7. For abrupt changes in wave direction, LTR reorientation is observed to lag wave direction by  $O(1 \text{ h})$ .

[63] 8. Ripple response time estimated from the ripple volume and the bed load transport rate, the latter computed using the Meyer-Peter and Müller formula, are comparable to values measured in the laboratory, particularly at high sediment transport rates. The predicted response times for LTRs are  $O(10 \text{ s})$ .

[64] 9. The  $O(10 \text{ s})$  predicted response time is compatible with the (dis)appearance of LTRs on wave period and wave group time scales reported by others in field experiments, but is several orders of magnitude shorter than the observed  $O(1 \text{ h})$  lag in the adjustment of LTR orientation to rapid changes in wave direction through large ( $15^\circ$  to  $20^\circ$ ) angles.

[65] 10. Sediment bypassing is suggested as a potential mechanism for reconciling the mismatch between the observed reorientation time and the predicted ripple adjustment time.

[66] 11. We argue that bed load bypassing necessarily occurs during ripple reorientation to create the bridging segments and new spatial scales introduced during orientation adjustment. We also suggest that the three dimensionality of the evolving ripple pattern could result in additional bypassing by diverting bed load into suspension.

[67] Several directions for future work are indicated by the results presented here. Direct measurements of sediment flux and bottom stress are needed, not only during quasi-steady conditions, but also during active ripple adjustment to changing forcing conditions, to test the validity of the bypassing hypothesis. Additional realizations of ripple response to rapidly changing wave directions should be sought. Explanations for the discrepancy between measurements of anorbital ripple occurrence in the field and in prototype-scale laboratory facilities must be found. Numerical simulations of ripple reorientation should be explored.

[68] **Acknowledgments.** The authors would like to thank the FRF staff for granting access to the bathymetry and 8 m wave directional spectra as well as Richard Cheel for providing the shoaled FRF wave directions and the wave directional spectra from the EM flowmeter and pressure sensor data. We also thank Tom O'Donoghue and John Sleath for sending us their ripple adjustment time data. This research was funded by the Coastal Geosciences Program of the U.S. Office of Naval Research and the Natural Sciences and Engineering Research Council of Canada.

## References

- Cacchione, D. A., and D. E. Drake (1979), A new instrument system to investigate sediment dynamics on continental shelves, *Mar. Geol.*, *30*, 299–312.
- Cheel, R. A., and A. E. Hay (2008), Cross ripple patterns and wave directional spectra, *J. Geophys. Res.*, *113*, C10009, doi:10.1029/2008JC004734.
- Clifton, H. E. (1976), Wave-formed sedimentary structures: A conceptual model, in *Beach and Nearshore Sedimentation*, edited by R. A. Davis Jr. and R. L. Ethington, *Spec. Publ. Soc. Econ. Paleontol. Mineral.*, *24*, 126–148.
- Clifton, H. E., and J. R. Dingle (1984), Wave-formed structures and paleoenvironmental reconstruction, *Mar. Geol.*, *60*, 165–198.
- Conley, D. C., and D. L. Inman (1992), Field observations of the fluid-granular boundary layer under near-breaking waves, *J. Geophys. Res.*, *97*(C6), 9631–9643.
- Crawford, A. M., and A. E. Hay (2001), Linear transition ripple migration and wave orbital velocity skewness: Observations, *J. Geophys. Res.*, *106*(C7), 14,113–14,128.
- Davis, J. P., D. J. Walker, M. Townsend, and I. R. Young (2004), Wave-formed sediment ripples: Transient analysis of ripple spectral development, *J. Geophys. Res.*, *109*, C07020, doi:10.1029/2004JC002307.
- Dingle, J. R., and D. L. Inman (1977), Wave-formed ripples in nearshore sands, in *Proceedings of the 15th Coastal Engineering Conference*, vol. 2, pp. 2109–2126, Am. Soc. of Civ. Eng., New York.
- Doucette, J. S., and T. O'Donoghue (2006), Response of sand ripples to change in oscillatory flow, *Sedimentology*, *53*, 581–596.
- Fofonoff, N. (1969), Spectral characteristics of internal waves in the ocean, *Deep Sea Res. Oceanogr. Abstr.*, *16*, 58–71.
- Fredsoe, J., and R. Deigaard (1992), *Mechanics of Coastal Sediment Transport*, 369 pp., World Sci., Singapore.
- Gindikin, S. G. (1992), Some notes on the Radon transform and integral geometry, *Monatsh. Math.*, *113*, 23–32.
- Hanes, D. M., V. Alymov, Y. X. Chang, and C. Jette (2001), Wave-formed sand ripples at Duck, North Carolina, *J. Geophys. Res.*, *106*(C10), 22,575–22,592.
- Hay, A. E., and T. Mudge (2005), Primary bed states during SandyDuck97: Occurrence, spectral anisotropy, and the bed state storm cycle, *J. Geophys. Res.*, *110*, C03013, doi:10.1029/2004JC002451.
- Hay, A. E., and D. L. Wilson (1994), Rotary sidescan images of nearshore bedform evolution during a storm, *Mar. Geol.*, *119*, 57–65.
- Henderson, S. M., and A. J. Bowen (2002), Observations of surf beat forcing and dissipation, *J. Geophys. Res.*, *107*(C11), 3193, doi:10.1029/2000JC000498.
- Herbers, T. H. C., S. Elgar, and R. T. Guza (1999), Directional spreading of waves in the nearshore, *J. Geophys. Res.*, *104*(C4), 7683–7693.
- Hubbell, D. W. (1964), Apparatus and techniques for measuring bedload, *U.S. Geol. Surv. Water Supply Pap.*, *1748*.
- Huntley, D., G. Coco, K. R. Bryan, and A. B. Murray (2008), Influence of “defects” on sorted bedform dynamics, *Geophys. Res. Lett.*, *35*, L02601, doi:10.1029/2007GL030512.
- Inman, D. L. (1957), Wave-generated bedforms in nearshore sands, *Tech. Rep. 100*, U.S. Army Corps of Eng., Washington, D. C.
- Maier, I. (2008), Linear transition ripples in nearshore sands, M.S. thesis, 99 pp., Dalhousie University, Halifax, N. S., Canada.
- Meyer-Peter, E., and R. Müller (1948), Formulas for bed-load transport, in *Report on the Second Meeting of the International Association for Hydraulic Structures Research*, pp. 39–64, Stockholm.
- Mogridge, G. R., and J. W. Kamphuis (1972), Experiments on bed form generation by wave action, in *Proceedings of the Thirteenth Coastal Engineering Conference*, pp. 1123–1142, Am. Soc. of Civ. Eng., Vancouver, B. C., Canada.
- Mogridge, G. R., M. H. Davies, and D. H. Willis (1994), Geometry prediction for wave-generated bedforms, *Coastal Eng.*, *22*, 255–286.
- Newgard, J. P., and A. E. Hay (2007), Turbulence intensity in the wave boundary layer and bottom friction under (mainly) flat bed conditions, *J. Geophys. Res.*, *112*, C09024, doi:10.1029/2006JC003881.
- Nielsen, P. (1992), *Coastal Bottom Boundary Layers and Sediment Transport*, 324 pp., World Sci., River Edge, N. J.
- O'Donoghue, T., J. S. Doucette, J. J. van der Werf, and J. S. Ribberink (2006), The dimensions of sand ripples in full-scale oscillatory flows, *Coast. Eng.*, *53*, 997–1012, doi:10.1016/j.coastaleng.2006.06.008.
- Park, S. J., M. B. Ahmad, R. Seung-Hak, S. J. Han, and J. A. Park (2004), Image corner detection using Radon transform, in *Computational Science and Its Applications - ICCSA 2004, LNCS*, vol. 3046, edited by A. Laganà et al., pp. 948–955, Springer, Berlin.
- Ribberink, J. S. (1998), Bed-load transport for steady flows and unsteady oscillatory flows, *Coast. Eng.*, *34*, 59–82.
- Rubin, D. M., and R. E. Hunter (1982), Bedform climbing in theory and nature, *Sedimentology*, *29*, 121–138.
- Sleath, J. F. A. (1984), *Sea Bed Mechanics*, 335 pp., John Wiley, New York.
- Smith, D., and J. F. A. Sleath (2005), Transient ripples in oscillatory flows, *Cont. Shelf Res.*, *25*, 458–501, doi:10.1016/j.csr.2004.10.012.
- Smyth, C., and A. E. Hay (2002), Wave friction factors in nearshore sands, *J. Phys. Oceanogr.*, *32*(12), 3490–3498.
- Smyth, C., and M. Li (2005), Wave-current bedform scales, orientation, and migration on Sable Island Bank, *J. Geophys. Res.*, *110*, C02023, doi:10.1029/2004JC002569.
- Smyth, C., A. E. Hay, and L. Zedel (2002), Coherent doppler profiler measurements of near-bed suspended sediment fluxes and the influence of bedforms, *J. Geophys. Res.*, *107*(C8), 3105, doi:10.1029/2000JC000760.
- Soulsby, R. L., and R. J. S. Whitehead (2005), Prediction of ripple properties in shelf seas: Mark 2 predictor for time evolution, *Tech. Rep. TR 154*, HR Wallingford, Wallingford, U. K.
- Swart, D. (1974), Offshore sediment transport and equilibrium beach profiles, *Tech. Rep. 131*, Delft Hydraul. Lab., Delft, Netherlands.
- Testik, F. Y., S. I. Voropayev, and H. J. S. Fernando (2005), Adjustment of sand ripples under changing water waves, *Phys. Fluids*, *17*(7), 07214, doi:10.1063/1.1946768.

- Thornton, E. B., and R. T. Guza (1983), Transformation of wave height distribution, *J. Geophys. Res.*, 88(C10), 5925–5938.
- Traykovski, P. (2007), Observations of wave orbital scale ripples and a nonequilibrium time-dependent model, *J. Geophys. Res.*, 112, C06026, doi:10.1029/2006JC003811.
- Traykovski, P., A. E. Hay, J. D. Irish, and J. F. Lynch (1999), Geometry, migration, and evolution of wave orbital ripples at LEO-15, *J. Geophys. Res.*, 104, 1505–1524.
- Voropayev, S. I., G. B. McEachern, D. L. Boyer, and H. J. S. Fernando (1999), Dynamics of sand ripples and burial/scouring of cobbles in oscillatory flow, *Appl. Ocean Res.*, 21, 249–261.
- Wiberg, P. L., and C. K. Harris (1994), Ripple geometry in wave-dominated environments, *J. Geophys. Res.*, 99(C1), 775–789.
- 
- A. E. Hay and I. Maier, Department of Oceanography, Dalhousie University, 1355 Oxford St., Halifax, NS B3H 4J1, Canada. (alex.hay@dal.ca)